# HIGH PRECISION ACCELEROMETER CONTACT MICROPHONES FOR DETECTION OF MECHANO-ACOUSTIC CARDIOPULMONARY SIGNALS

A Dissertation
Presented to
The Academic Faculty

by

Pranav Gupta

In Partial Fulfillment
of the Requirements for the Degree
Master's Degree in the
School of Electrical and Computer Engineering

Georgia Institute of Technology
August 2020

# HIGH PRECISION ACCELEROMETER CONTACT MICROPHONES FOR DETECTION OF MECHANO-ACOUSTIC CARDIOPULMONARY SIGNALS

Approved by:

Dr. Farrokh Ayazi, Advisor
School of Electrical and Computer Engineering
*Georgia Institute of Technology*

Dr. Omer T. Inan
School of Electrical and Computer Engineering
*Georgia Institute of Technology*

Dr. Azadeh Ansari
School of Electrical and Computer Engineering
*Georgia Institute of Technology*

Date Approved: July 20, 2020

# ACKNOWLEDGEMENTS

First, I would like to express my sincerest thanks to my advisor, Dr. Farrokh Ayazi. His extensive knowledge of engineering and design, insightfulness during conversations, passion for novel research, and mentorship have been a great source of inspiration. Additionally, I would like to acknowledge Dr. Omer Inan and Dr. Azadeh Ansari for their time and consideration as members of my thesis committee.

I would like to acknowledge Yaesuk Jeong and Jaehoo Choi with whom I worked closely to develop and characterize the MEMS devices, as well as Mark Faingold with whom I worked to implement the wearable prototype. I was privileged to work with such hardworking, creative, and positive teammates. To the members of the IMEMS Research Lab – your help, support, and friendship have been invaluable to my experience as a graduate student.

Lastly, I would like to thank my friends and family who have provided continuous and unconditional love, support, and encouragement.

# TABLE OF CONTENTS

# LIST OF TABLES

# LIST OF FIGURES

# LIST OF SYMBOLS AND ABBREVIATIONS

| | |
|---|---|
| MEMS | Micro-electromechanical systems |
| ACM | Accelerometer Contact Microphone |
| SCG | Seismocardiogram |
| HARPSS | High Aspect Ratio Combined Poly and Single crystal Silicon |
| CPD | Cardio-Pulmonary Diseases |

# SUMMARY

The objective of this research is to design, fabricate and characterize a MEMS-based Accelerometer Contact Microphone (ACM) that enables wearable measurement of cardiopulmonary mechano-acoustic signals, providing a platform for longitudinal monitoring of vital health parameters. This work presents a hermetically-sealed low noise, wide bandwidth out-of-plane accelerometer comprising of sub-micron transduction gap (270nm) electrodes implemented using HARPSS+ process, which is fabricated and characterized as a contact microphone. The sensor is designed using a cantilever topology, with a resonant frequency of 13.6kHz and sensitivity of 14.2fF/g. The fabricated sensor is interfaced with a commercial capacitance readout circuit, and a low noise performance with a noise density of 127μg/√Hz and a bias instability of 22μg is measured. A high sensitivity of 76mV/g is recorded by placing the ACM is on a shaker table and applying 1-g sinusoidal acceleration. The ACM is packaged at atmospheric pressure, reducing its operational bandwidth from its measured resonant frequency of 12.5kHz down to 640Hz. The use of the ACM in a body-worn auscultation system is validated by mounting it on the chest, and non-invasively recording acoustic emissions produced within the thoracic cavity. The recorded signals are filtered and processed to extract the phonocardiogram, seismocardiogram, lung sounds, and chest wall motion using data processing techniques, demonstrating the possibility of accurately capturing multiple types of acoustic and vibrational data from the body simultaneously using a single sensor. The efficacy of the ACM is further highlighted by its ability to compute vital health parameters such as heart rate and heart rate variability with accuracy comparable to a medical-grade ECG system.

# CHAPTER 1. INTRODUCTION

## 1.1 Cardiopulmonary Diseases (CPD)

Cardiopulmonary diseases (CPD) are the leading cause of mortality globally, and the interdependency of cardiac and pulmonary health makes continuous monitoring of cardiopulmonary parameters essential for an accurate and timely diagnosis. Patients suffering from CPD experience abnormal heart rate and rhythm, chest pain, shortness of breath and fatigue. Additionally, chronic coughing and wheezing of lungs is often developed as a secondary condition arising due to cardiac dysfunction[1]. There is a growing incidence of CPD amongst the aging population globally, leading to high mortality rates, increased medical expenses and significant degradation of quality of life of affected individuals. Statistics show that cardiovascular diseases account for deaths of over 600,000 Americans annually, while chronic pulmonary disorders are responsible for over 150,000 deaths each year. By 2030, about 43% of the population is projected to suffer from some form of CPD[2].

An effective strategy to improve survival rate is to detect the early onset of CPD and slow its progression with preventive care and preemptive treatments[3][4]. This requires use of wearable health monitoring platforms for longitudinal monitoring of vital parameters leading to accurate diagnosis. Initial physiological markers of developing CPD are presence of abnormal heart sounds and adventitious breathing sounds. The use of an auscultation device such as a stethoscope is considered as the first step in clinical evaluation of these conditions and a very powerful tool available to physicians[5].

## 1.2 Auscultation: Basic Diagnostic Practice

Auscultation is the practice of listening to sounds emanating from a body using tools such as a stethoscope. To date, the practice of auscultation has remained unchanged and is considered as the basic diagnostic method for health evaluation by doctors around the globe. However, the auscultation tool – the stethoscope – has continuously evolved since its invention by René Laennec in 1816.

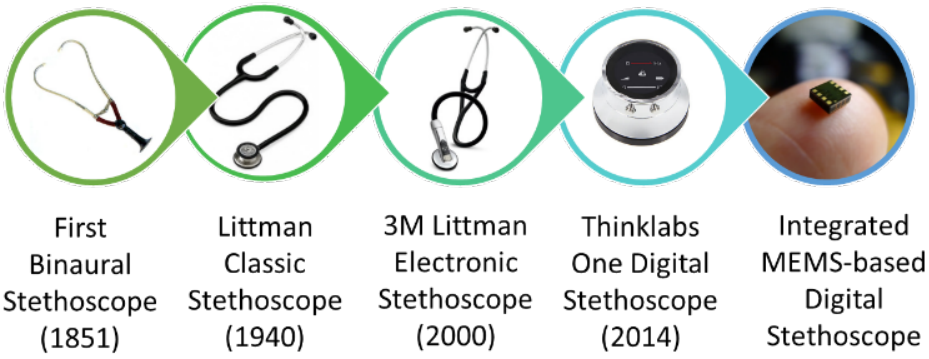


**Figure 1 – Evolution of the stethoscope**

The stethoscope offers a cost-effective and accurate method for early detection of cardiopulmonary dysfunction. In comparison to electrocardiogram (ECG), the stethoscope enables detection of structural abnormalities in the heart valves and defects in the cardiopulmonary system that are characterized by adventitious sounds. While imaging techniques such as echocardiogram, magnetic resonance imaging (MRI), and computed tomography (CT) scan offer high-resolution images of the organs, they require expensive equipment and specialized personnel to operate these complex machines. This limits their use in a bed-side monitoring environment[6].

There is a growing demand for high performance electronic auscultation devices due to their ability to augment traditional clinical equipment for instance, by allowing the physicians to remotely diagnose and track patient health post-treatment. Capturing body motion coupled with the auscultation data can allow physicians to correlate cardiopulmonary sounds to daily activities. Additionally, monitoring the timing of abnormal breath sounds with respect to respiratory cycle is of great interest to doctors for accurate diagnosis[7].

Typical electronic stethoscopes use membrane-type microphones which operate by generating an electrical response to pressure changes in air caused by sound waves. This technique is susceptible to environmental noise and may suffer due to insufficient acoustic energy transfer. The piezoelectric-type stethoscope produces electrical signals due to distortion of a piezo-crystal coupled to the stethoscope diaphragm. Again, due to distortion, this technique does not accurately capture the sound and resultant output may differ from the original tone [6]. Moreover, performance of such microphones is limited by their size [8] and are unable to capture low frequency signals such as respiratory rate and body motion.

However, despite the recent advancements in stethoscope design and operation, these devices continue to remain bulky and are not suitable for application in a wearable and ambulatory setting. This has resulted in the use of stethoscopes being confined to a clinical setting, making it imperative to visit a physician for basic auscultatory diagnosis. The short-term monitoring of cardiopulmonary sounds is inadequate for a comprehensive diagnosis as several characteristic acoustic signatures such as pathological ventricular gallops, or adventitious breath sounds may not appear under sedentary conditions, making it difficult

to accurately identify the disease. Moreover, quantification of auscultation sounds is not standardized and is highly dependent on the physician's experience, making auscultation highly susceptible to human error. Hence, to overcome these challenges, we require a miniaturized, wearable auscultation tool that can be applied reliably under ambulatory conditions for long-term monitoring of these cardiopulmonary sounds.

### 1.3 Physiology of the Cardiopulmonary System

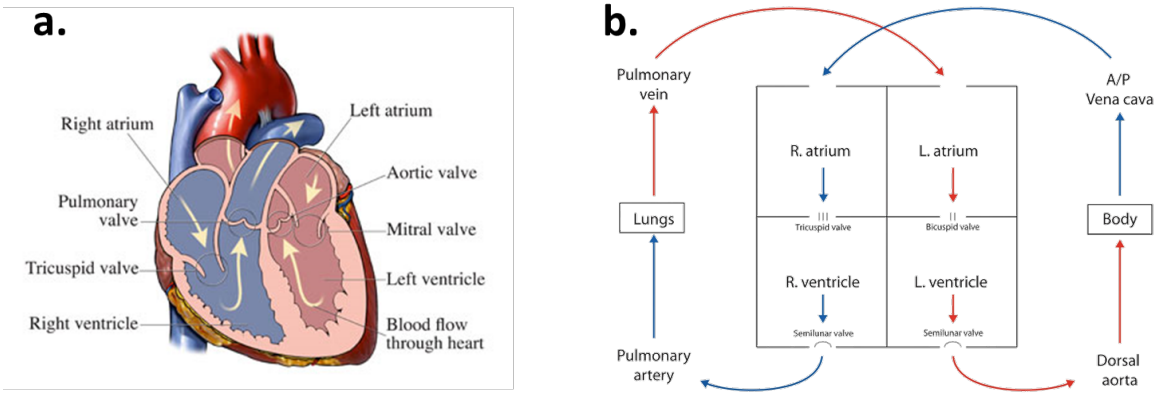


**Figure 2 – (a) Anatomy of the heart (b) Blood flow in the cardiopulmonary system**

The anatomic structure of the heart is comprised of four chambers: the right atrium, the right ventricle, the left atrium, and the left ventricle as shown in Figure 2. Heart valves present at the entrance and exit of these chambers regulate the flow of the blood in the forward direction while preventing backward regurgitant flow. These valves are composed of leaflets, with the tricuspid and semilunar valve consisting of three leaflets each, while the mitral valve comprises of two leaflets. The vibration of these cardiac structures results in hemodynamic changes and turbulent blood flow, consequently creating vibrational waves which travel through the chest wall and can be heard using a stethoscope [9]. The turbulent flow is affected by the fluid viscosity, density, velocity, and the diameter of the

blood vessels, providing a unique acoustic signature for various cardiovascular dysfunction.

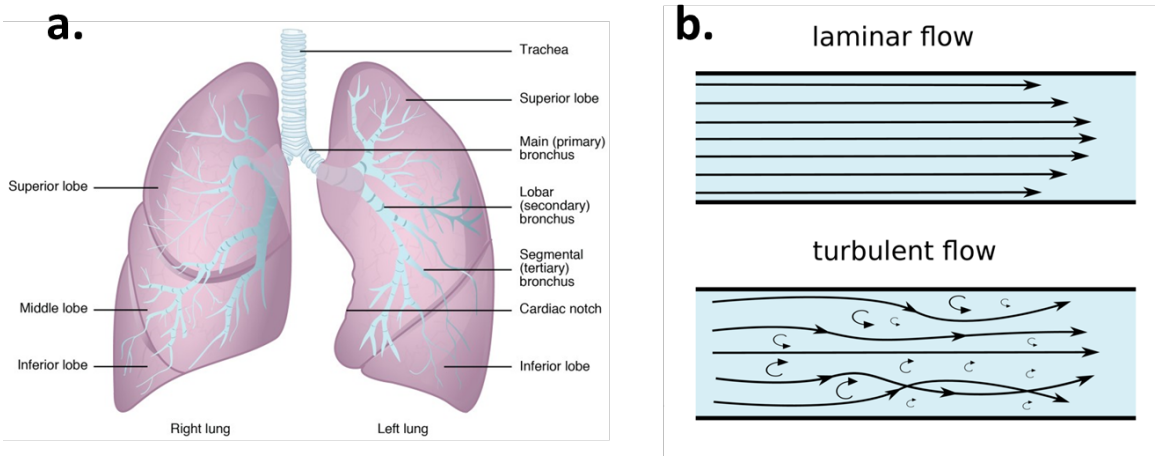


**Figure 3 – (a) Anatomy of the lungs (b) Types of air flow profile**

The lungs occupy the major volume of the thoracic cavity and are responsible for the oxygenation of the blood. Each lung is composed of smaller units called lobes, which are separated by Fissures. The right lung consists of three lobes: the superior, middle, and inferior lobes. The left lung consists of two lobes: the superior and inferior lobes, as shown in Figure 3. The inhaled air accesses the lungs via the trachea. The trachea branches out into the bronchi inside the lungs, which further consist of the alveoli at the edges, wherein the oxygen-rich air is absorbed by the blood.

The characteristic features of the air flow are modulated as it passes through these pulmonary structures, resulting in production of breath sounds. The two main types of air flow seen in the lungs are the laminar and turbulent airflow. Laminar flow occurs when the streams of airflow are parallel to the walls and the central streams moves faster than air in the peripheral streams, resulting in low frequency, silent vibrations. The turbulent flow

occurs in as the air passes through airways with irregular walls, such as the trachea and bronchi. The airflow is disorganized and chaotic, producing high frequency audible sounds during the respiratory cycle [7]. The outer lining of the lungs and chest wall act as a low-pass filter, not allowing high frequency sounds to pass through. Therefore, the sound heard over the chest wall consists mainly of low frequencies, with harmonics occurring up to a few kilohertz signal.

## 1.4 Classification of Cardiopulmonary Sounds

### *1.4.1 Cardiac Sounds*

The cardiac sounds can be classified into two broad categories: Normal and abnormal heart sounds, as shown in the Figure 4. These can be further classified using four characteristic features namely – timing, intensity, duration, and frequency. The occurrence of the cardiac sounds provides an insight to the functioning of the organ and are closely related to the opening and closing of heart valves, along with turbulent blood flow. They generally exhibit low characteristic frequencies, in the range of 20-500Hz [10], and are best heard at the intercostal spaces, and the apex of the heart.

The normal heart sounds, comprising of $S_1$ and $S_2$, define systole and diastole period and form the basis for analyzing all cardiac auscultations. $S_1$ occurs due to closing of the atrioventricular valves (Mitral and Tricuspid), while $S_2$ occurs due to closing of the semilunar valves (Aortic and Pulmonary).

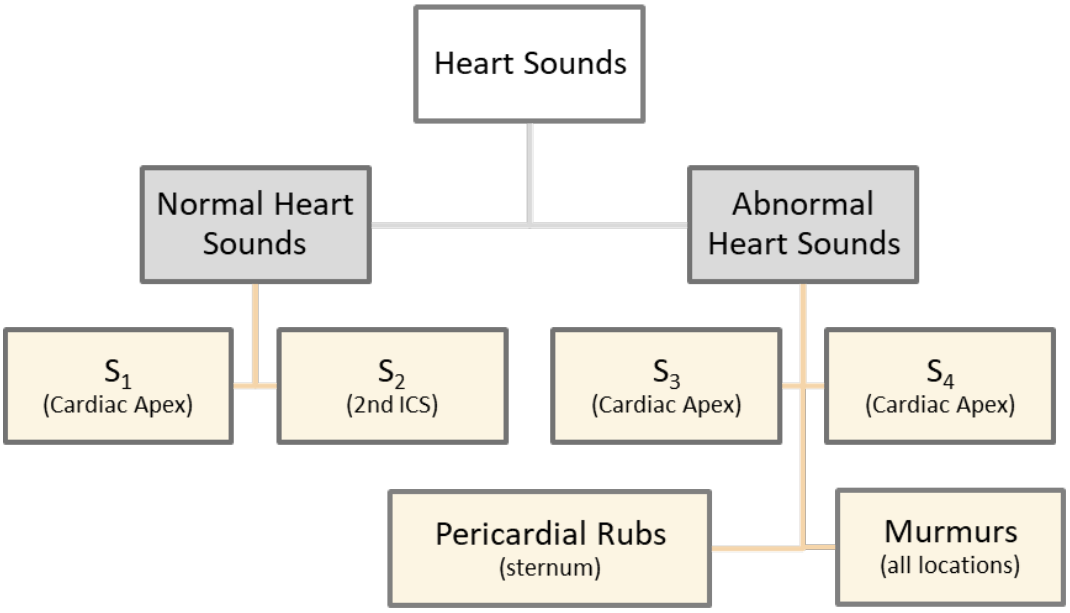


**Figure 4 – Classification of Cardiac Sounds**

The first heart sound ($S_1$) occurs as the mitral and tricuspid valves close at the onset of ventricular systole and is most prominently heard at the apex and the fourth left intercostal space. It exhibits higher amplitude and longer duration amongst all cardiac sounds. The $S_1$ sound lasts for a period of 100–200ms, with its frequency components in the range of 10-200 Hz. The commonly perceived abnormalities of $S_1$ correspond to its intensity – with the sound varying in intensity with every beat. The primary variables governing intensity of $S_1$ are strength of ventricular contraction and the position of the atrioventricular leaflets at the onset of ventricular systole [10].

The second heart sound ($S_2$) occurs at the onset of the ventricular diastole and can be clearly heard at the second or third left intercostals space. Its occurrence coincides with the completion of the T-wave of the electrocardiogram (ECG). The $S_2$ sound consists of two high-frequency components, occurring due to the closure of the aortic valve and the closure

of the pulmonary valve. While the intensity of $S_2$ has less diagnostic importance, the 'splitting' of the two high frequency components provides valuable information. In healthy subjects, the split between these two components increases by 20-30 milliseconds [10]. These characteristic features assist physicians in diagnosing pulmonary hypertension and ischemic heart disease.

The third and fourth heart sounds, also collectively called the gallop sounds, originate due to rapid ventricular filling but exhibit different characteristics and clinical significance. These sounds occur at low frequencies (20-70 Hz) and are best heard using bell of the stethoscope. The third heart sound ($S_3$), occurs in the early diastolic phase and is considered pathological in older adults above the age of 40. Presence of these sounds in young people is generally physiological. It appears about 120-180ms after the occurrence of the $S_2$ heart sound, and provides clinical indications of developing congestive heart failure, and valvular regurgitation. The fourth heart sound (S4) occurs in the late diastolic phase (just before $S_1$) and is closely associated with hypertension and fibrosis caused by stiffness of the heart tissue.

Along with the third and fourth heart sounds, presence of other abnormal heart sounds such as murmurs and clicks function as biomarkers for developing cardiac dysfunction. Characteristic features of these sounds include their location, timing and frequency. The sound intensity of these abnormal murmurs during the respiratory cycle provide vital information regarding the functioning of the heart valves [10].

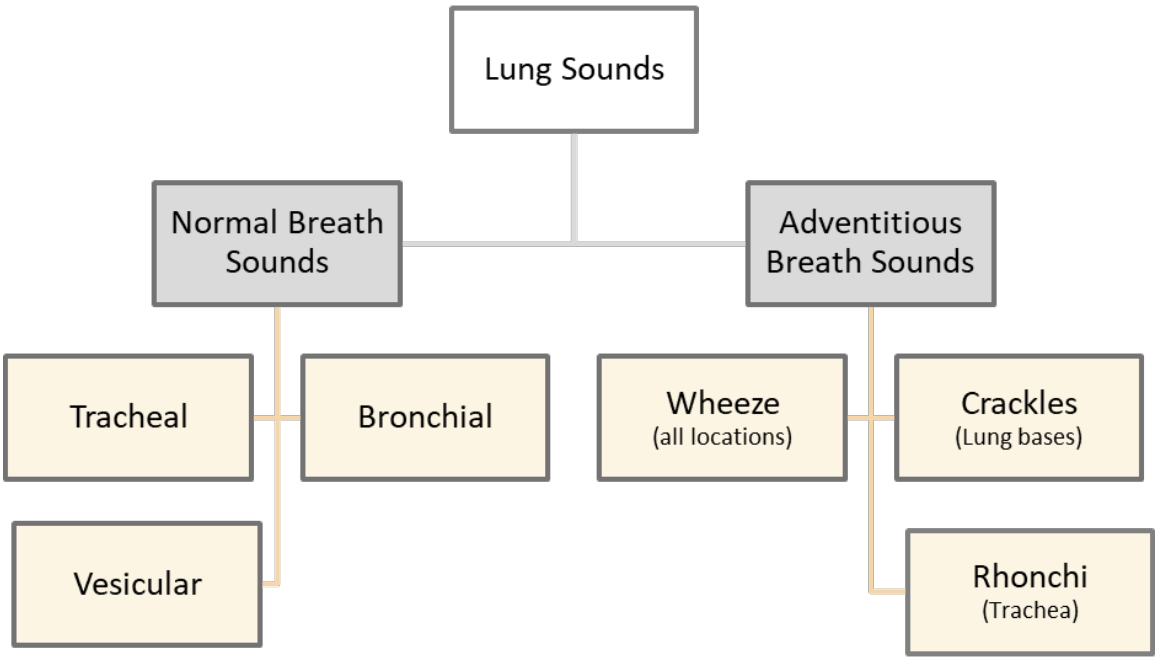


**Figure 5 – Classification of Pulmonary Sounds**

*1.4.2 Pulmonary Sounds*

Pulmonary sounds are broadly categorized as normal and adventitious breath sounds, as shown in the Figure 5. Patients exhibiting diminished or adventitious breath sounds such as crackles, wheezes, and rhonchi, may be diagnosed with conditions such as pneumonia and chronic pulmonary disorder. The adventitious respiratory sounds often occur in conjunction with the regular breath sounds and require a highly skilled physician for differentiating the weak acoustic signatures.

Normal or tracheal breathing sounds originate in the upper airways in the trachea and are produced due to turbulent airflow in the bronchi and trachea. These sounds are continuous in nature and range in a frequency range of 100-1500Hz [11]. The characteristic

features of such sounds are that they are loud and tubular and nonmusical in nature. These can be heard during both – the inhalation and exhalation – phase of respiration. They are often used to monitor patients with sleep apnea.

Vesicular sounds mostly occur during the inspiratory phase and are characterized by low frequency (below 100Hz) and low intensity sounds. These generally occur at the posterior bases of the lungs, with the inhalation phase sound occurring for longer duration compared to the exhalation phase sound [11].

Bronchial breathing sounds originate in the central airways in the lobar regions and are caused due to turbulent flow vortices along the airways. These sounds continuous in nature and range in a frequency range of 600-1000Hz [11]. The characteristic features of such sounds are that they are soft and nonmusical in nature. They are often used to monitor patients with consolidated lung tissue (e.g. Pneumonia) or fibrosis.

Crackles are discontinuous adventitious respiratory sounds, occurring in a frequency range of 100-2000Hz with a small duration (~20ms). These are commonly heard in patients exhibiting obstruction or fluid accumulation in lungs. Wheezes are continuous and musical adventitious respiratory sounds occurring for short durations (~80-100ms) in the frequency range 100-1000Hz, with certain harmonics present at higher frequencies. These sounds can be monophonic or polyphon and are often used a key indicator of developing asthma [10], [11].

## 1.5 Detection of Cardiopulmonary Sounds

To continuously monitor these mechano-acoustic cardiopulmonary sounds over extended periods of time we require wearable sensing systems which are non-invasive, simple and cost-effective[12]–[17]. These signals convey physiological parameters that are essential for a comprehensive evaluation of the health status of individuals[18], [19]. For instance, the opening and closing of the heart valves, along with pumping of blood into the arteries and veins, produce acoustic signals in the frequency range of 20-1000 Hz[20], [21]. The existence of pathological sounds in these signals can indicate structural defects in the heart valves, blockage in arteries or ventricular dysfunctions[22], [23]. In addition, micro-vibrations of the chest wall in the low frequency range of DC-100 Hz are linked to mechanical cardiac events and contain information about valve functionalities and cardiac muscle contractility[24], [25]. Moreover, changes in the lung volume during the respiratory cycle cause macro-motions of the thorax and abdomen with ultralow frequency below 1 Hz[26]. This signal is useful to extract the respiratory pattern, which is significant in predicting clinical deterioration of patients with chronic airflow obstruction[27], [28], and diagnose several other respiratory diseases[29].

These mechano-acoustic signals comprise a wide range of intensities and frequencies; requiring, ultrasensitive sensors with high dynamic range and wide bandwidth to record these signals with high fidelity. In addition, these sensors must be small and lightweight to be easily accommodated in a wearable platform. This enables continuous monitoring of cardiopulmonary system over extended period of time and facilitates early detection and comprehensive diagnosis[14]–[16], [30]. Existing systems including digital stethoscopes and accelerometers are not well-suited for low-profile, wearable and high-

precision monitoring systems. Digital stethoscopes rely on large size membranes to acquire weak acoustic signals emanating from the body. Miniature accelerometers with low-bandwidth have been used in limited capacity to obtain mechanical vibrations and record SCG signals and respiratory patterns[31], [32] but fail to detect characteristic acoustic signatures of ventricular dysfunction such as pathological $S_3$ heart sounds occurring in patients with congestive heart failure, and adventitious pulmonary sounds associated with deteriorating cardiopulmonary conditions[7], [19], [23]. While preliminary studies using accelerometers in implantable defibrillators has been reported for monitoring cardio-mechanical signals in heart failure patients[33], these devices are unsuitable for preventive care as they require expensive and complex surgical procedures for implantation.

An effective approach to tackle these challenges is using a capacitive accelerometer contact microphone (ACM). A micro-g accelerometer with large bandwidth ($f_{res}$ >10 kHz) and low noise (<10 μg√Hz) out-of-plane sensitivity functions as a contact microphone. By having a high resonant frequency, the accelerometer can pick up μg-level accelerations produced by acoustically vibrating structures. Such a microphone is not sensitive to air-borne acoustic emissions, but only sensitive to vibrations from its contact surface. Its small size allows it to replace bulky stethoscopes with ergonomic wearable auscultation systems that can precisely measure cardiopulmonary sounds, chest wall motion, seismocardiogram (SCG) signal as well as body motion of an individual simultaneously.

In this work, a low noise, wide bandwidth out-of-plane accelerometer with nano-gap (270nm) capacitive electrodes implemented using HARPSS+ process [34], [35] is designed, fabricated and characterized as a contact microphone. The performance of this accelerometer contact microphone is characterized using a shaker table, and the use of this

contact microphone as a body-worn auscultation device is validated by mounting it on the chest and recording sounds produced in the thoracic cavity. The recorded signals are filtered and processed to extract the heart sounds and SCG signal from the recorded data. Similarly, lung sound and chest wall motion are extracted using data processing techniques, demonstrating the possibility of accurately capturing multiple types of acoustic and vibrational data from the body at the same time.

# CHAPTER 2. ACCELEROMETER CONTACT MICROPHONE

## 2.1 General Operation Principle

An accelerometer contact microphone (ACM) is micro-sensor that unifies the functionality of an inertial device – an accelerometer – used for measuring activity and body motion, with an auscultatory sensor such as a microphone for capturing heart and lung sounds, into a single-chip device. The sensor exhibits an extremely high sensitivity in the out-of-plane direction, with a wide operational bandwidth, more than 10kHz, along with an ultra-low noise performance, having a noise density lower than 10 μg√Hz.

The general operation principle of the ACM can be described using a simplified lumped model, as shown in Figure 6, comprising of a proof mass *M* suspended in an accelerating reference frame via a mechanical spring *K* and damper *D*. Upon externally applied acceleration, the proof mass experiences a displacement *X*, which can be modeled using Newton's second law of motion, given by equation (1).

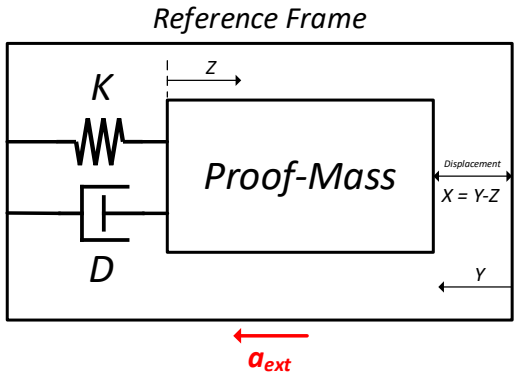


**Figure 6 – Simplified lumped model of the MEMS accelerometer contact microphone**

$$M\frac{d^2x}{dt^2} + D\frac{dx}{dt} + Kx = F_{ext} = -M\overrightarrow{a_{ext}} \tag{1}$$

$$x \approx \frac{M}{K}\overrightarrow{a_{ext}} = \frac{1}{\omega_0^2}\overrightarrow{a_{ext}} \tag{2}$$

$$\frac{x(s)}{F_{ext}(s)} = \frac{1}{Ms^2 + Ds + K} = \frac{{}^{1}/_{M}}{s^2 + {}^{\omega_0}/_{Q}\, s + \omega_0^2} \tag{3}$$

Since the motion of the proof mass is a second order equation, the operational bandwidth is determined by the fundamental resonant frequency $\omega_0$. To capture all acoustic vibrations, the ACM requires to have an operational bandwidth of at least 10 kHz. However, at such high resonant frequencies, the displacement of the proof-mass reduces significantly, to the order of nanometers. Detection of such small displacements using capacitive transduction is extremely challenging due to substantial degradation of the signal-to-noise ratio. Hence to overcome this challenge, the capacitive transduction gap size is scaled to sub-micron levels (~300nm), effectively increasing the ratio between displacement and capacitive transduction gap, to achieve a higher signal strength.

The operational bandwidth of the ACM is also dependent on the damping coefficient of the device, which is given by equation (4). The damping coefficient of the quasi-static capacitive accelerometer is primarily dictated by the squeezed-film-damping, occurring due to the interaction between the compressed air-molecules and the microstructure, and is given by equation (5). Here $N_e$ represents the number of electrodes, $\eta_{eff}$ is the viscosity of the ambient gas, $l_e$ is the electrode length, $h_e$ is the electrode thickness, and $d$ is the capacitive gap size.

$$\text{Bandwidth} = \omega_0 \sqrt{1 - 2\zeta^2 + \sqrt{2 - 4\zeta^2 + 4\zeta^4}} \tag{4}$$

$$D_{\text{squeeze-film}} = N_e \eta_{\text{eff}} l_e \left(\frac{h_e}{d}\right)^3 \tag{5}$$

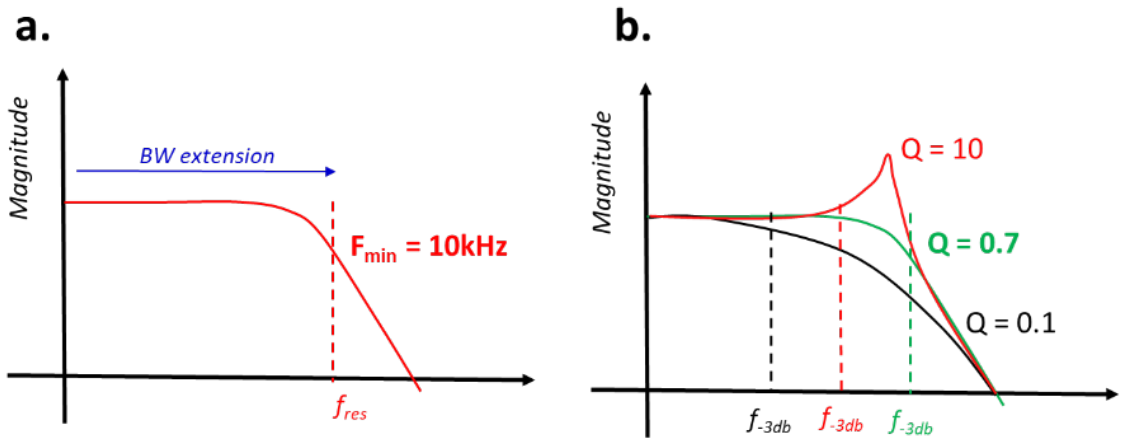


**Figure 7 – (a) Operational bandwidth requirement of the ACM with a minimum resonant frequency of 10kHz to accurately capture the acoustic vibrations. (b) Critically damped operation of the ACM (Q=0.7) to ensure maximum operational bandwidth.**

Since the squeeze-film damping is subject to the capacitive gap, by scaling down these gap sizes to sub-micron levels along with hermetically sealing the ACM in a low vacuum environment, we can precisely control the damping coefficient and achieve a critically-damped device with maximum operational bandwidth.

To capture all acoustic vibrations with high fidelity, the ACM must also have a low noise performance (<10 µg/√Hz) along with the wide bandwidth (>10kHz). Utilizing the nanoscale capacitive transduction gaps in ACM, we can overcome design challenges pertaining to tradeoffs between the operational bandwidth and noise performance experienced in conventional accelerometer design. The total noise of the ACM is given by

a combination of the mechanical and electrical components, namely the Brownian Noise Equivalent Acceleration (BNEA) and Circuit Noise Equivalent Acceleration (CNEA). These noise components can be analytically expressed as a function of the resonant frequency and transduction gap size and are given by equation (6) and (7).

$$\text{BNEA} = \sqrt{\frac{4k_b T\omega_0}{MQ}} \tag{6}$$

$$\text{CNEA} = \frac{\Delta C_{min}\omega_0^2 d^2}{2\varepsilon_0 A} \tag{7}$$

As per the equations of the BNEA and CNEA, the noise performance of the device scales proportionally to the resonant frequency and the transduction gap size. The increased noise level due to the desired wide operational bandwidth, is compensated by scaled-down sub-micron transduction gaps, enabling implementation of high-performance ACM devices with a small footprint, high sensitivity and wide operational bandwidth [36], [37].

## 2.2 ACM Sensor Design

An out-of-plane torsional cantilever topology [38] is chosen to implement the ACM, wherein the proof mass is supported by torsional tethers at one end, while the other end is free to rotate. To maintain a small form factor, the sense electrodes are placed within the proof mass area, and a differential top electrode configuration is employed to suppress common mode noises, as shown in Figure 8. This differential capacitance measurement is achieved by designing the sense electrodes such that the top poly-silicon is connected to the '-' sense electrode and overhangs the proof-mass to create the first transduction

capacitance, while at the '+' sense electrode the transduction capacitance is created with the top poly-silicon connected to the proof-mass and overhanging the sense electrode area. When acceleration occurring due to acoustic vibrations is applied orthogonal to the device, generated torque will rotate the proof-mass, changing the capacitance between sense electrodes and proof-mass, as shown in Figure 9.

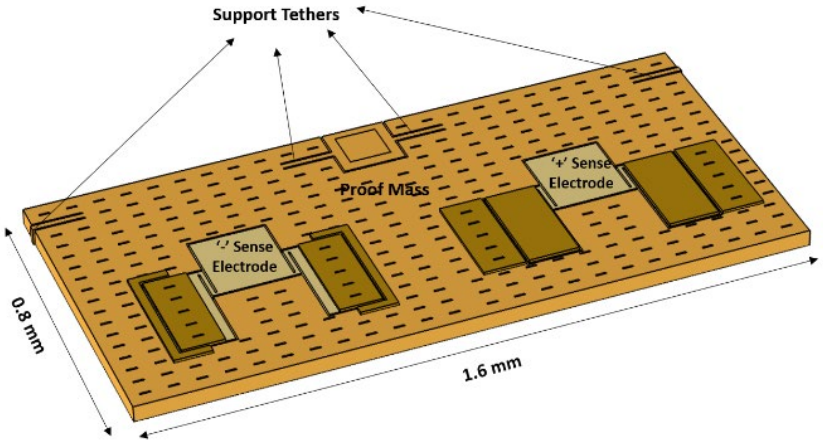


**Figure 8 – COMSOL simulation of ACM device structure. The proof mass is supported by support tethers at one end and houses the '+' and '-' sense electrode within its footprint. Top polysilicon is used to create differential sensing topology.**

The dimensions of the proof-mass are determined such that the mechanical noise of the ACM is minimized, and the length of the device remains much greater than the width to maximize the restoring force. Use of such a design topology ensures low stiction and high yield from the fabrication process. The resonant frequency exceeding 10kHz which is required by the ACM is achieved by fine-tuning the dimensions of the support tethers. Additionally, the placement of the tethers is done such that subsequent resonant modes occur at significantly higher frequencies. The operational resonant frequency of the ACM

is 13.6 kHz, with the successive resonant modes occurring at 82.6 kHz and 82.9 kHz, respectively. The simulated modes shapes of the device are shown in Figure 10.

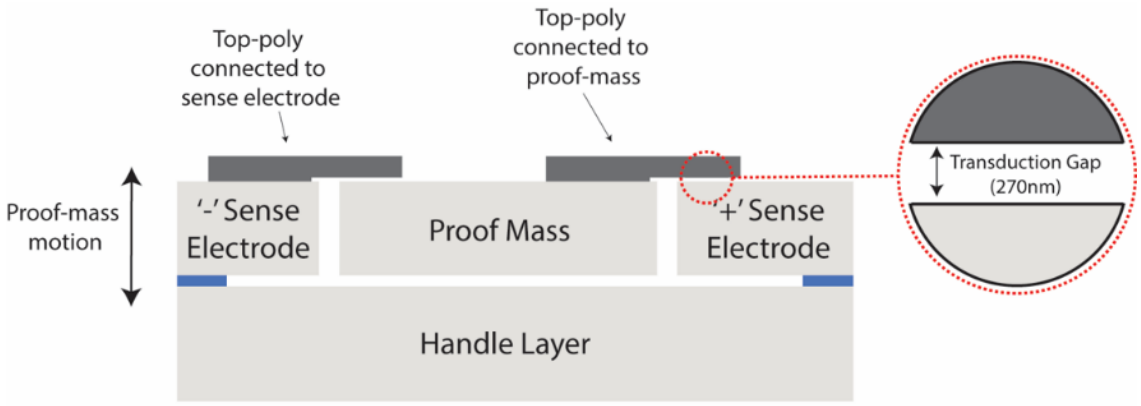


**Figure 9 – Schematic implementation of differential sensing topology using top-polysilicon electrodes and a 270nm transduction. Proof-mass moves perpendicular to the plane of the device.**

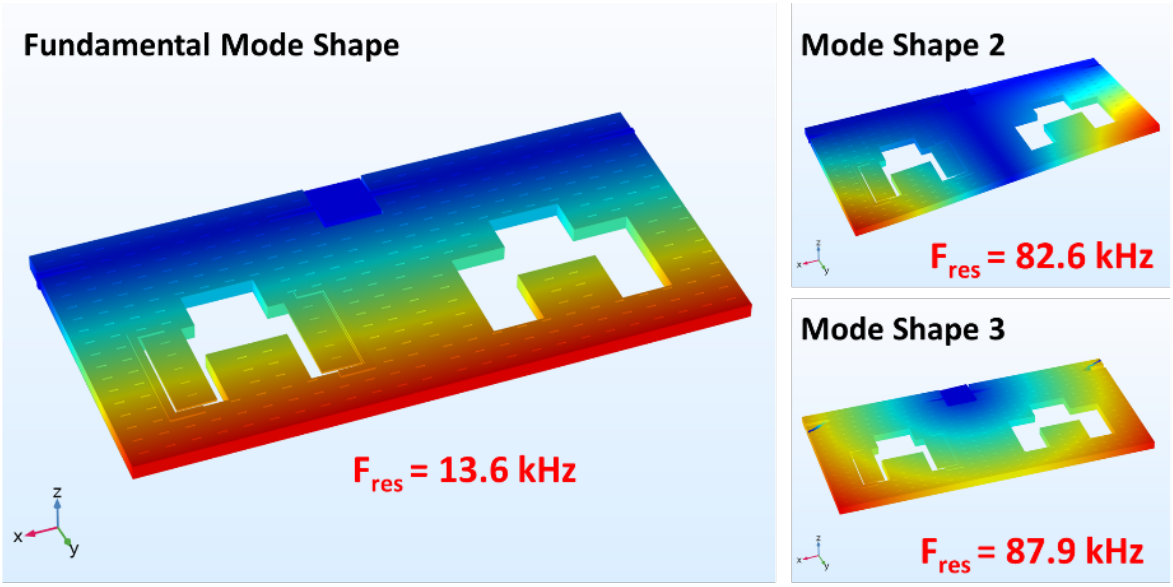


**Figure 10 – Simulated resonant mode shapes of the ACM. The fundamental mode shape is the primary mode of operation wherein the device acts as a cantilever and displaces in the out-of-plane direction. Subsequent mode shapes occur at much higher frequencies.**

Both the sense electrodes of the ACM are designed identically to maintain the center of mass of the device and minimize any process variations. They have sufficient transduction area to have equal capacitances of 1.7pF at each electrode to achieve a high scale factor. The '-' sense electrode is constructed with the polysilicon layer attached to the movable proof-mass and overhanging the fixed sensing electrode. On the other hand, the '+' sense electrode is constructed with the polysilicon attached to the fixed sense electrode and overhanging the moveable proof-mass. Hence, as the proof-mass displaces along the z-axis, the capacitance on each electrode changes as the transduction gap size increases or decrease, resulting in a differential readout of capacitance. The change in capacitance is characterized by increasing the bias voltage across the electrode. At an input bias voltage of 1V, the change in capacitance at each ACM electrode is 40.2fF, as shown in Figure 11. The overall scale factor for the ACM is obtained by combining the total change in capacitance for 1-g applied acceleration. The simulated scale factor for this device is 14.2fF/g, with the applied acceleration up to 16-g, as shown in Figure 12. The cross-axis sensitivity is less than 0.1% along both orthogonal axes.

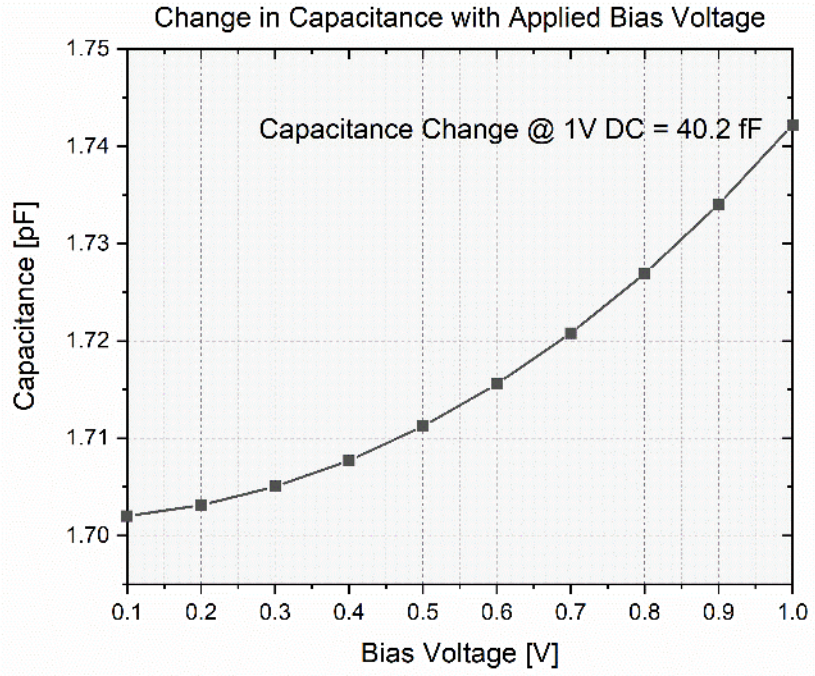


**Figure 11 – Change in capacitance with increasing applied bias voltage across each sensing electrode.**

Since the operational bandwidth of the ACM is dependent on the resonant frequency, damping coefficient and packaging pressure level, a finite-element simulation is conducted to accurately identify these parameters. For maximum bandwidth, the device must operate in a critically damped condition with a damping coefficient of 0.707. Varying the pressure from low vacuum conditions of 10 Torr pressure to an atmospheric pressure of 760 Torr changes the operational bandwidth as shown in Figure 13. At atmospheric pressure, the operational bandwidth is reduced to 640Hz, while at low vacuum pressure an underdamped condition is obtained extending the bandwidth to the higher frequencies.

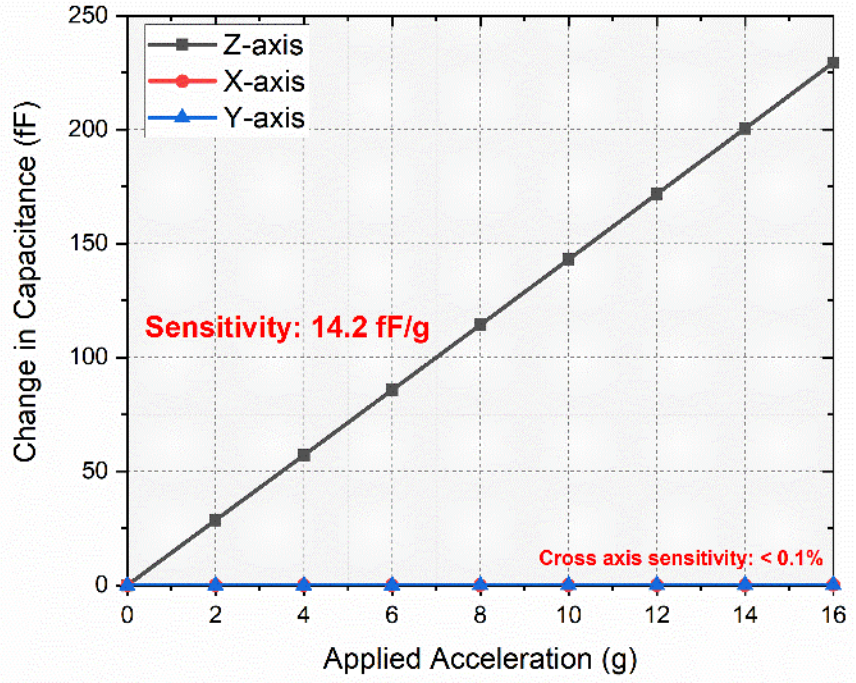


**Figure 12 – Simulated scale factor of the ACM device. The device has a sensitivity of 14.2fF/g in the out0-of-plane direction, with a cross-axis sensitivity of <0.1% along both orthogonal axes.**

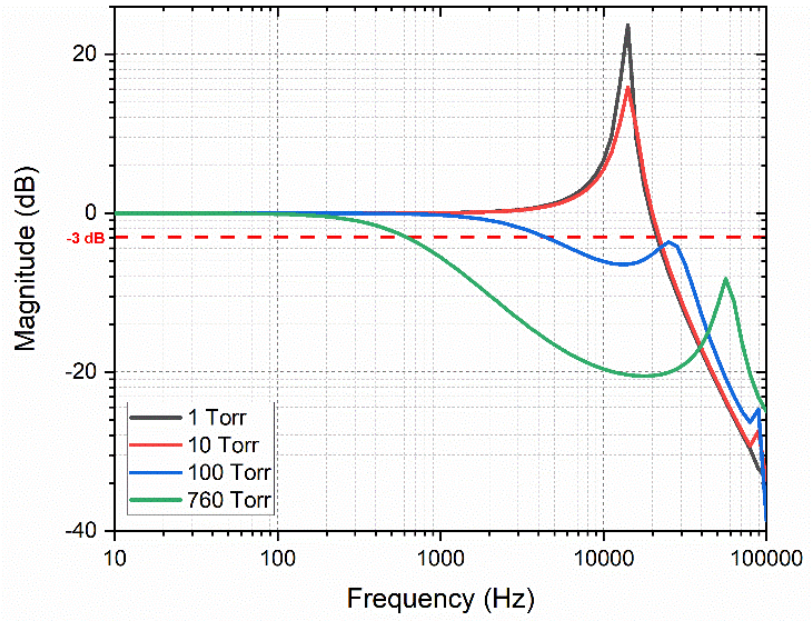


**Figure 13 – Simulated operational bandwidth of the ACM at varying pressure levels. The device operates in an overdamped condition at atmospheric pressure (760 Torr) with an operational bandwidth of 640Hz.**

## 2.3 Fabrication

The device is fabricated using the HARPSS+ process on an SOI (Silicon-on-Insulator) wafer having 40µm thick device layer with ~270nm capacitive gaps [34], [35]. After the releasing process, the completed wafer is then wafer-level packaged using eutectic bonding to a silicon capping wafer with built-in through-silicon-vias (TSV). Figure 14 shows the SEM of the uncapped ACM device and the device cross section with a 270nm transduction gap.

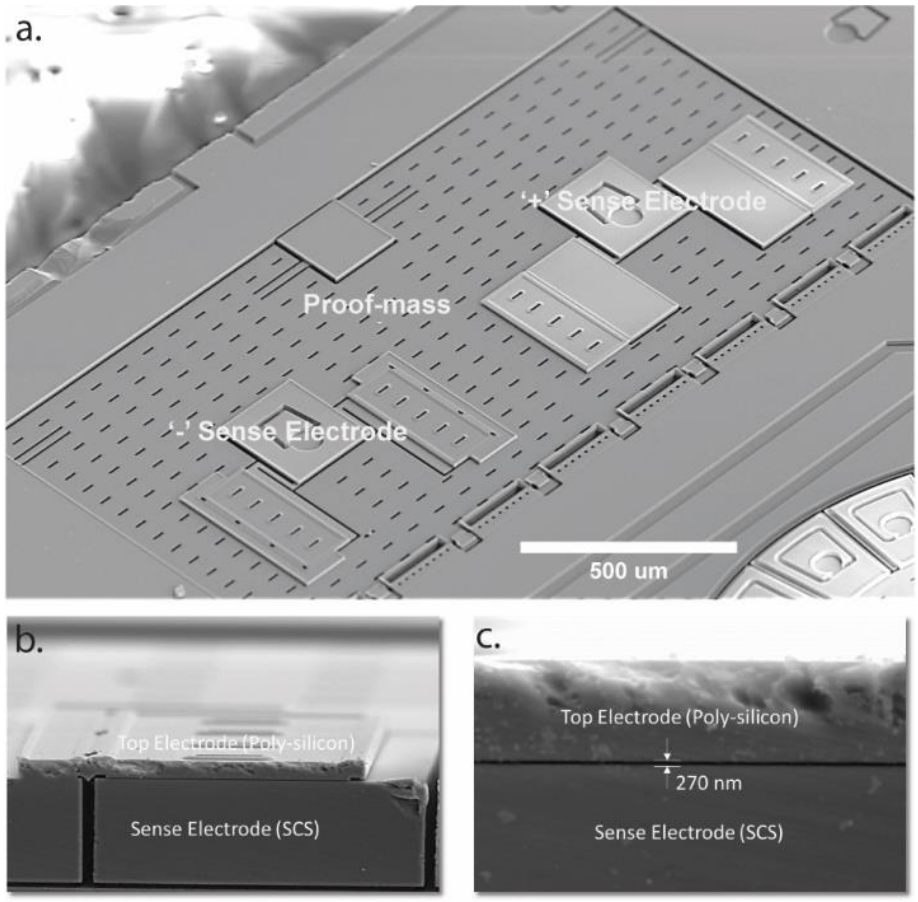


**Figure 14 – (a)SEM photograph of the fabricated ACM device showing the proof-mass and sensing electrodes. (b) Cross-sectional image of the sensing electrode displaying the thin top-poly electrode overhanging the single-crystal silicon (SCS) sense electrode in the device layer. (c) close-up view of the cross-sectional image demonstrating the 270nm transduction gap.**

# CHAPTER 3. SENSOR CHARACTERIZATION

## 3.1 Evaluation Board Development

The fabricated ACM microsensor is interfaced with MS3110P – a commercially available off-the-shelf capacitance readout circuit – that exhibits low capacitive resolution (4aF/√Hz) along with a wide bandwidth (programmable up to 8kHz). A miniature evaluation board is developed by utilizing both sides of a 4-layered circuit board to ensure a small factor, which is essential to eliminate any undesired resonant frequency arising due to the circuit board during tests under high frequency vibrations. The differential electrode pair of the MEMS device are wire-bonded to the CS1IN and CS2IN pins of the circuit, while the CSCOM pin is connected to the device layer. The handle layer of the MEMS device is connected to ground.

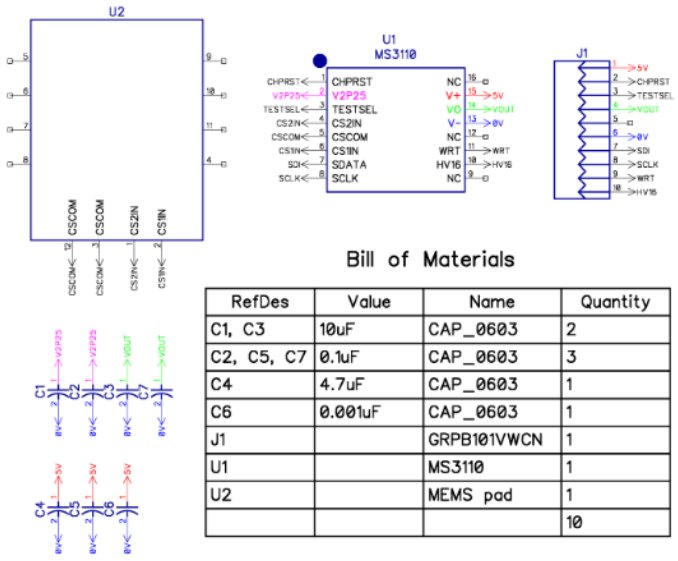


Bill of Materials

| RefDes | Value | Name | Quantity |
|---|---|---|---|
| C1, C3 | 10uF | CAP_0603 | 2 |
| C2, C5, C7 | 0.1uF | CAP_0603 | 3 |
| C4 | 4.7uF | CAP_0603 | 1 |
| C6 | 0.001uF | CAP_0603 | 1 |
| J1 | | GRPB101VWCN | 1 |
| U1 | | MS3110 | 1 |
| U2 | | MEMS pad | 1 |
| | | | 10 |

**Figure 15 – Schematic of miniature evaluation board designed for test and characterization of the ACM.**

The top-side of the evaluation board, housing the wire-bonded wafer-level-packaged MEMS devices, is covered in a thin layer of clear epoxy potting compound DP270 (manufactured by 3M) as shown in Figure 16. The 2-part epoxy (consisting of the base and accelerator) is mixed in a ratio 1:1 by volume and cured at room temperature for 24 hours. This epoxy layer protects the bonding wires from damage against handling and allows the MEMS sensor to be placed directly over the testing surface, thus achieving good vibrational coupling. Additionally, the epoxy protects the device from detrimental environmental effects such as moisture.

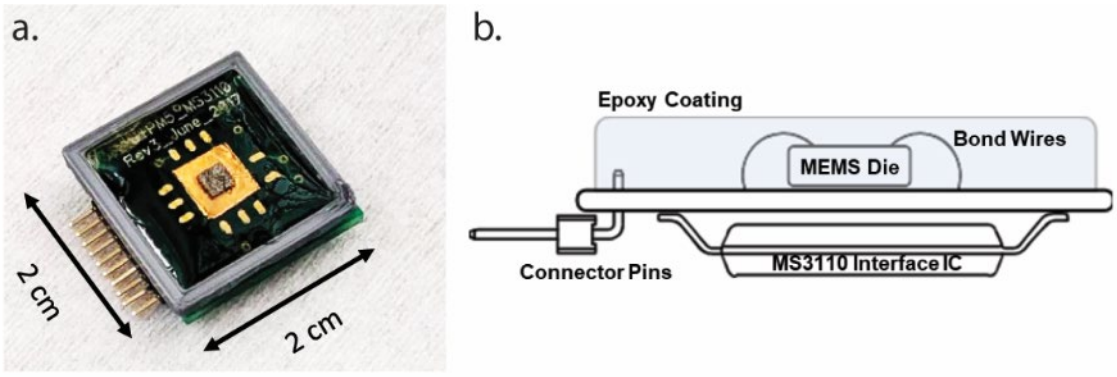


**Figure 16 – (a) Fabricated and assembled ACM evaluation board on a miniature PCB (2cm x 2cm) with the MEMS die placed on top-side and the interface electronics on the bottom-side of the PCB. (b) Cross-sectional schematic diagram of the PCB demonstrating the location of all components. A protective epoxy layer is placed on top of the MEMS die.**

### 3.2 Environment Setup and Testing

Characterization of the fabricated ACM device is carried out by performing a series of tests with respect the sensitivity, dynamic range, bandwidth, and noise performance. The measured data is then compared to the simulation results to validate the design.

The evaluation board – comprising of the MEMS and MS3110P – provides an analog output voltage proportional to the applied acceleration, which is determined by the capacitance-voltage (C-V) gain setting of the readout circuit. The programmability of the readout circuit allows the user to choose the desired gain setting by varying the feedback capacitance. A C-V gain setting of 4.28mV/fF was set for all characterization results. A high precision 16-bit data acquisition unit (NI-9220 by National Instruments) is used to record the output voltage.

### *3.2.1 C-V Measurement Test*

Prior to interfacing the ACM to the readout circuit, it is essential to determine the functionality of the MEMS device. This is accomplished by measuring the capacitance across the electrodes and the proof mass of the accelerometer using an LCR meter. The measured nominal capacitance value is compared to the simulated capacitance value, while considering the effect of the capping wafer along with parasitic capacitances that may arise due to the circuit board. Then, a bias voltage is applied to simulate an external acceleration and the changes in the capacitance values are noted. Figure 17 demonstrates the change in capacitance as the bias voltage increases from 0 to 1 V. A nominal capacitance of 3.3pF on both electrodes is observed, with a change of 50fF at 1 V DC bias.

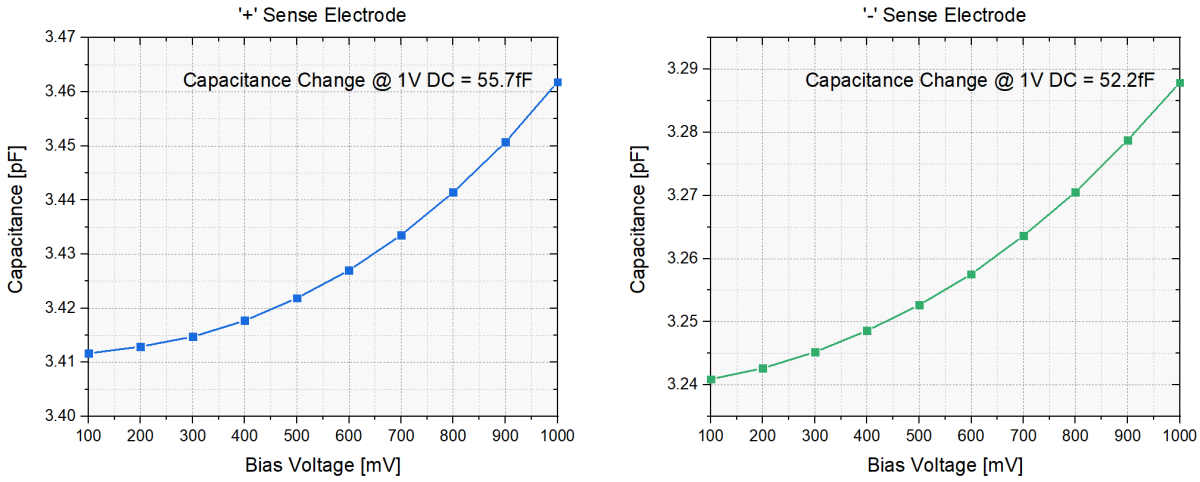


**Figure 17 – Capacitance-Voltage measurements demonstrating the change in capacitance as we increase the bias voltage between the proof-mass and sense electrodes. Measurements done using an LCR meter.**

### *3.2.2 Sensitivity Test*

To measure the sensitivity ($S_Z$), a shaker table (ET-126 HF by Lab Works Inc.) is used to apply a precise 1-g sinusoidal acceleration perpendicular to the plane of the device, and a peak voltage of 72.6mV/g is observed as shown in Figure 18. Additionally, the applied acceleration levels are increased up to 16-g to demonstrate the wide dynamic range of the sensor. To measure the cross-axis sensitivity ($S_{XZ}$, $S_{YZ}$), the evaluation board is then placed perpendicular to the shaker table. The measured cross-axis sensitivity is less than 3%, which arises mainly due to the misalignments occurring during placement of the MEMS die on the evaluation board and during placement of the board on the shaker table.

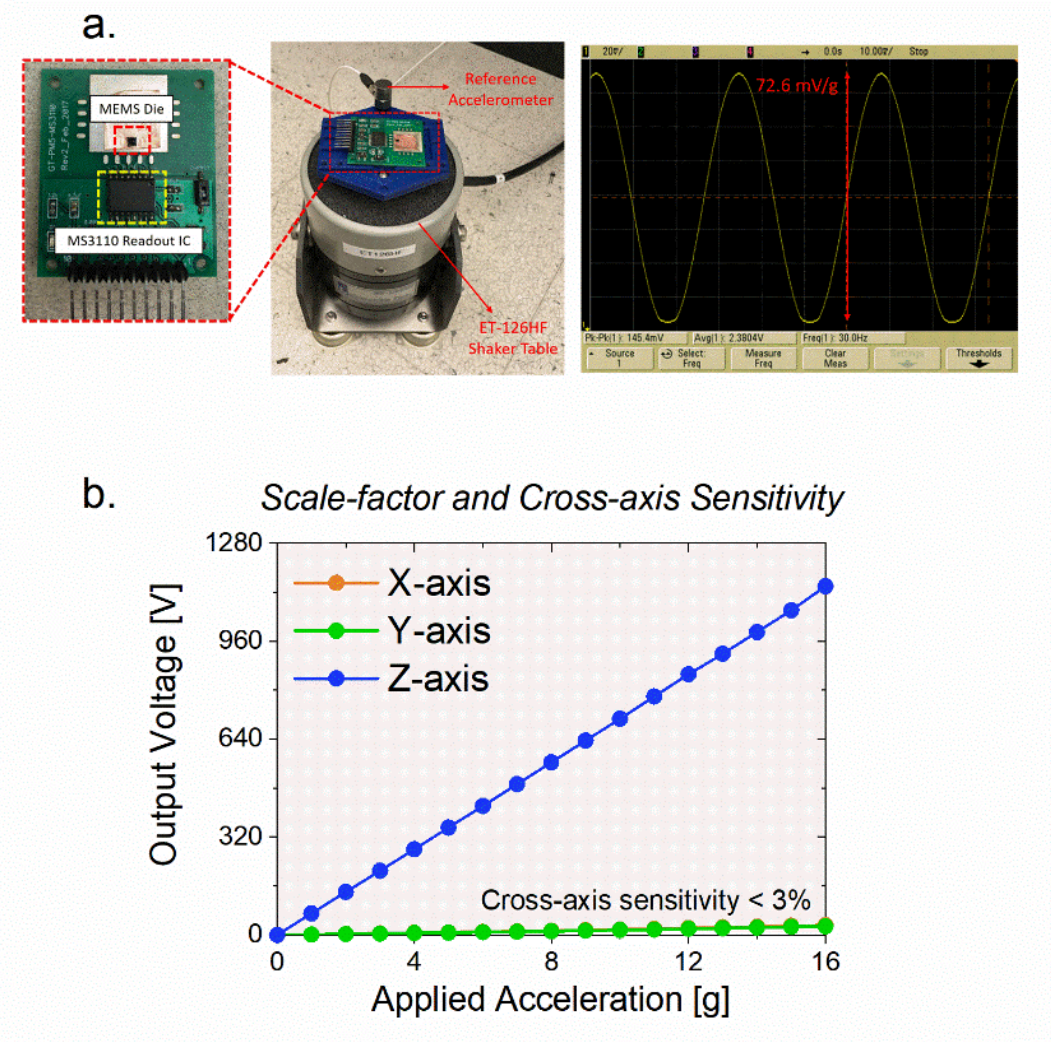


**Figure 18 – (a) Placement of an ACM evaluation board on the ET-126HF shaker table. A sinusoidal acceleration signal of 1g at 30Hz frequency is applied. Corresponding output waveform is plotted using an oscilloscope, demonstrating a sensitivity of 72.6mV/g. (b) Accelerations up to 16g are applied using the shaker table and output voltages are recorded, demonstrating a high dynamic range of the ACM.**

### *3.2.3 Noise Performance*

The noise performance of the sensor is characterized by placing it in under 0-g acceleration along its primary axis and recording the output for a long duration. The output voltage is used to plot the Allan Deviation Plot (as shown in Figure 19), demonstrating a low noise performance of 127µg/√Hz and a bias instability of 22µg. However, the system

is limited by the capacitive resolution of the interface circuit, and the noise performance can be further improved by utilizing a custom-made ASIC for optimal operation of the designed MEMS device.

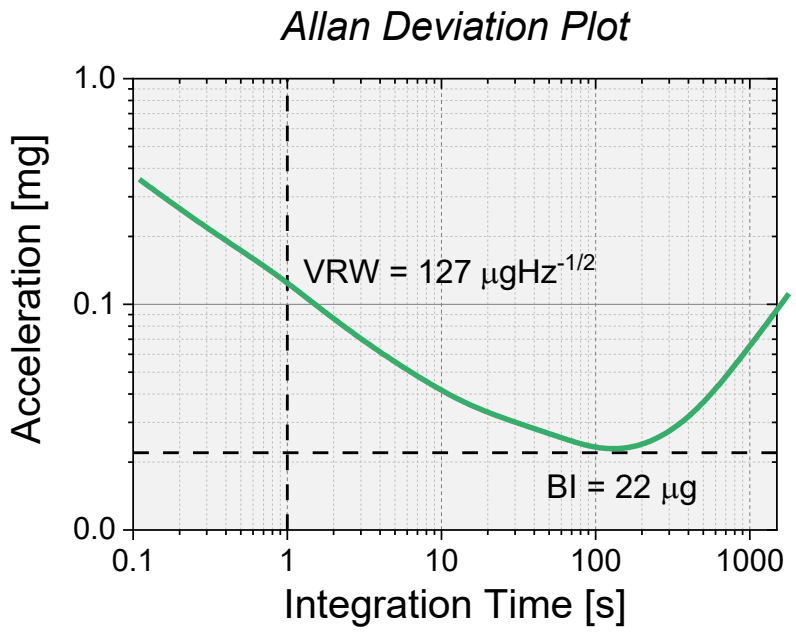


**Figure 19 – Allan deviation plot demonstrating the low noise performance of the ACM, showing a velocity random walk of 127μg/√Hz and a bias instability of 22μg.**

### *3.2.4 Resonant Frequency and Operational Bandwidth*

Since the ACM is a second-order system, its operational bandwidth is determined by resonant frequency of the device. The resonant frequency is measured by placing the device in a vacuum chamber and using a network analyzer to detect the resonant peak. The measured resonant frequency is 12.5 kHz, as shown in Figure 20. However, since the device operates at atmospheric pressure, the operational bandwidth is attenuated. This is measured by placing the evaluation board on the shaker table and recording the output voltage at varied input acceleration frequencies. Figure 20 shows the transfer function of

the device with an operational bandwidth of 640 Hz, which is in good agreement with the simulated operational bandwidth.

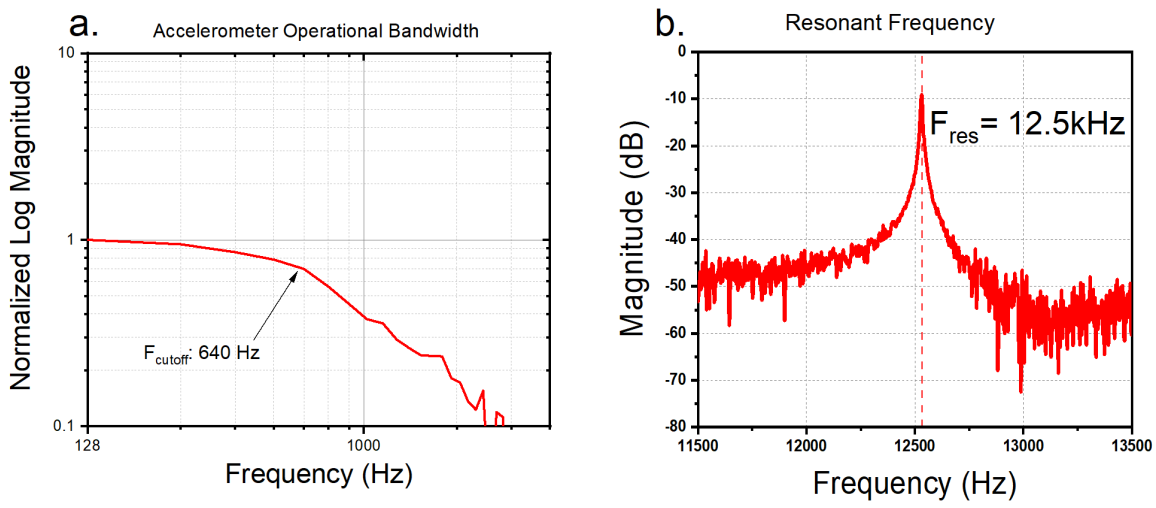


**Figure 20 – (a) The operational bandwidth of 640Hz of the ACM measured by sweeping the input acceleration frequency using a shaker table. (b) The resonant peak at 12.5kHz indicating the high operational bandwidth that can be achieved with vacuum packaging using this device.**

**Table 1 – Performance Summary of the ACM**

| Parameter | Value |
|---|---|
| Sensitivity | 76 mV/g |
| Resonant frequency | 12.5 kHz |
| Operational Bandwidth | 640 Hz |
| Linear dynamic range | 160 m/s$^2$ (16 g) |
| Die size | 2 mm×2 mm×1 mm |
| Gap size | 270 nm |
| Measured Noise density | 127 μg/√Hz (@ 1 Hz) |
| Brownian Noise of MEMS | 3.6 μg/√Hz (@10 Torr Pressure) |
| Measured Cross axis sensitivity | <3% |

# CHAPTER 4. BODY-WORN AUSCULTATION DEVICES

## 4.1 Sensor Placement

Several auscultation locations for cardiopulmonary sounds are available in the intercostal spaces (ICS) (i.e. the space between two consecutive ribs) on the chest. Cardiopulmonary sounds, which lie between 20 to 2500 Hz frequency range[39], are recorded by mounting the sensor left of the sternum in the 5th intercostal space, shown in Figure 21. The PCB is held in place using a chest strap to provide firm contact between the board and skin. Such configuration is essential to pick-up high-fidelity audio signals.

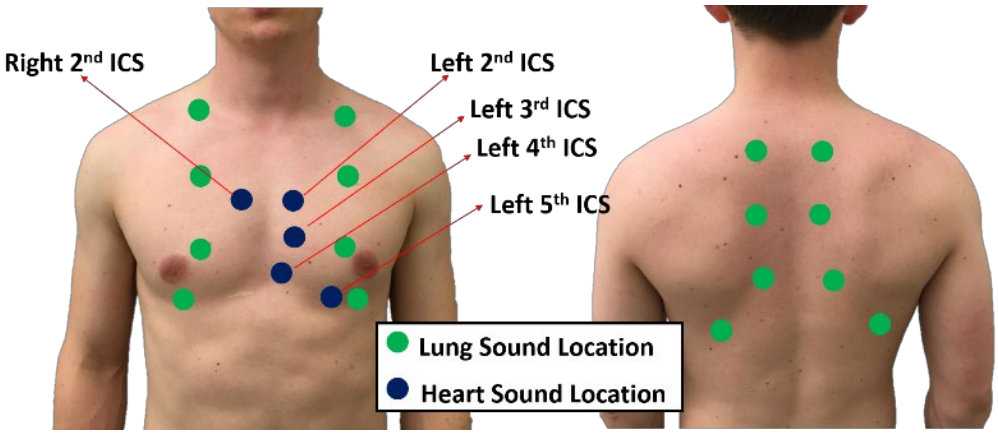


**Figure 21 – Sensor locations for placement of the ACM for auscultation applications.**

## 4.2 Cardiopulmonary Sound Sensing

The senor board is interfaced with NI-9220 DAQ to collect the data and a MATLAB program is used to filter the recorded signals which can be further stored in audio file format for playback. Unlike piezoelectric microphones, the ACM can measure accelerations down to DC level. This attribute is used to obtain additional information such

as body motion, heart rate, respiratory rate and even SCG signal. Moreover, using an array of the ACMs can result in high-precision activity detection of the user, thus providing an additional layer of information for correlation of auscultation to daily activities. The higher frequency components (> 20Hz) of the recorded signal correspond to the cardiopulmonary sounds.

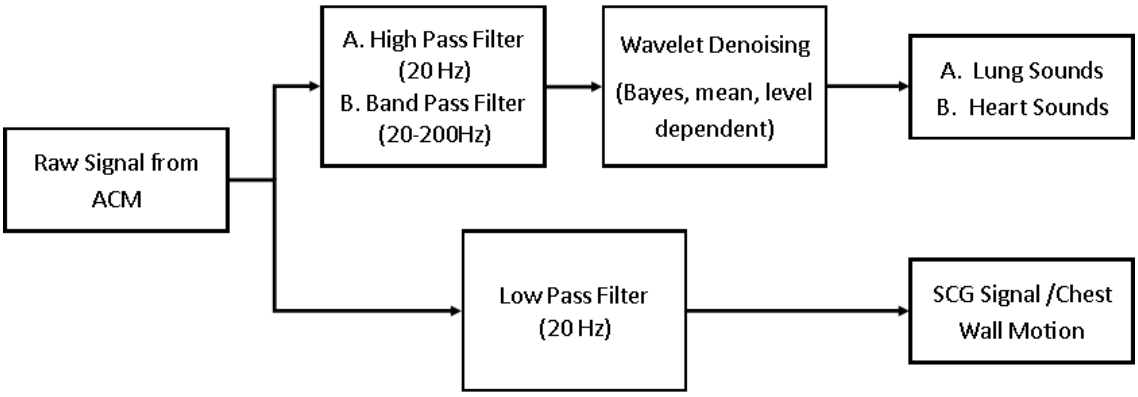


**Figure 22 – Signal processing and filtering algorithm used in extraction of useful information from the recorded ACM signal output.**

The filtering algorithm shown in Figure 22 is used to separate the low frequency component of chest wall motion and the high frequency component of the sound signal. The filtering is performed using high-order Butterworth filters on the basic criteria of audible (> 20Hz) and inaudible frequencies (< 20Hz). A wavelet denoising technique is used on the high frequency components to reduce noise and extract signal features[40]. The resultant waveforms are shown in Figure 23 and 24, corresponding to extracted cardiopulmonary signals.

There are two major cardiac sounds; $S_1$ and $S_2$, which occur due to closing of the atrioventricular valves (Mitral and Tricuspid) and closing of the semilunar valves (Aortic and Pulmonary), respectively. The period from $S_1$ to $S_2$ is known as Systole, whereas the

$S_2$ to $S_1$ period is known as Diastole [41], as shown in Figure 23. The recorded signal, known as phonocardiogram (PCG), is characterized by a 'lub-dub' sound, and provides a solid foundation for preliminary diagnosis, based on the frequency content and amplitude of the signal, of any cardiac disease.

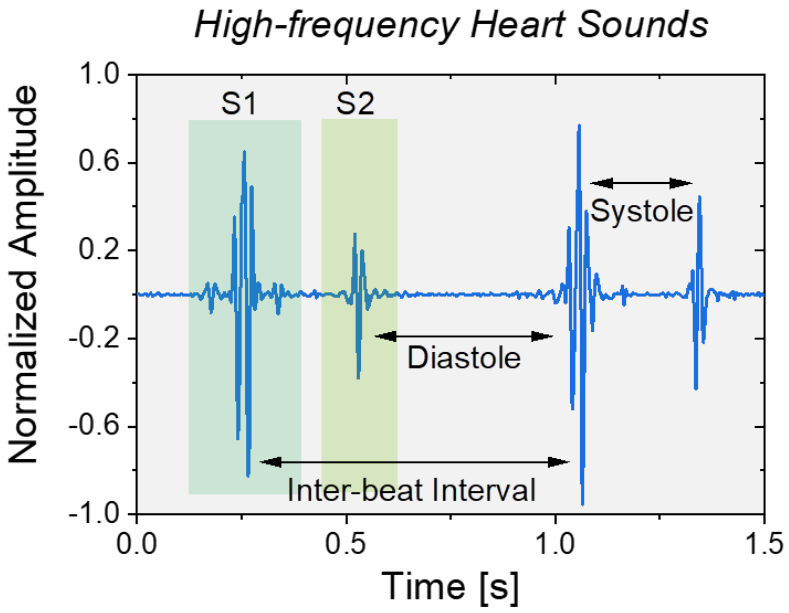


**Figure 23 – Recorded phonocardiogram signals of the heart demonstrating the two major heart sounds.**

Another feature captured along with the heart sounds is the SCG signal, defined as the micro-movements of the chest due to the pumping of blood at every heartbeat[24]. As this signal lies in the frequency range of 0-20Hz, it is typically captured using a precision micro-g accelerometer. The dual nature of the proposed contact microphone enables the detection of the SCG signal, while measuring cardiac sounds, as shown in Figure 24. The importance of capturing this waveform is marked by its unobtrusive nature and ability to detect early onset of several diseases such as acute myocardial disease, asymptotic coronary artery disease and congestive heart failure[42].

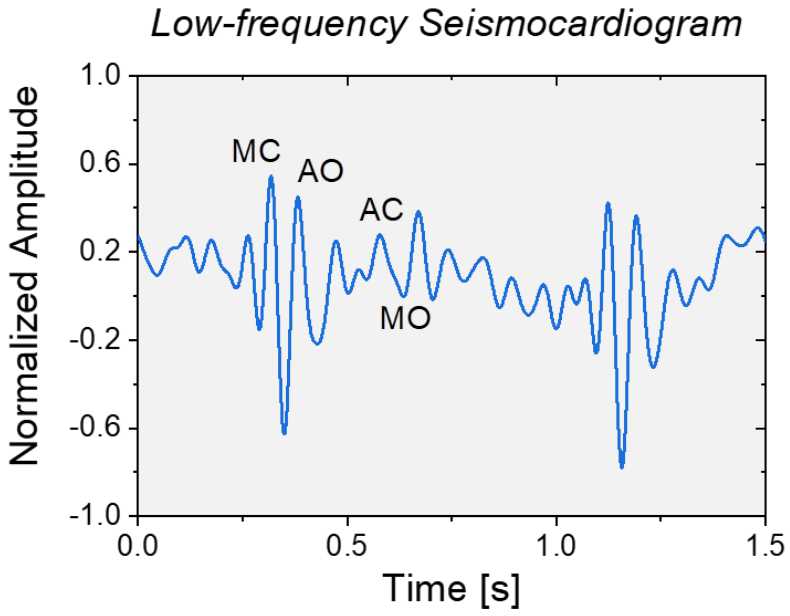


**Figure 24 – Recorded seismocardiogram (SCG) signal demonstrating the peaks corresponding to the opening and closing of the heart valves with each heartbeat.**

Auscultation of the lungs provides vital information regarding their physiology such as obstructions in airway or presence of liquid in the organ. The qualities of breath sounds modify as air passes through the lungs. The pitch and duration of recorded lung sounds differ with respect to location of the senor. The presence of adventitious breath sounds such as crackles or wheezes usually indicate disease[19]. To accurately identify the timing of abnormal breath sounds within a respiratory cycle, the inspiration and expiration can be monitored by tracking the movement of the chest wall. Normal “vesicular” breath sound recorded by our accelerometer contact microphone is shown in Figure 25 and 26.

The ACM demonstrates high-fidelity cardiopulmonary auscultation sensing capability as well as high sensitivity towards motion artifacts. Characteristic features of heart sounds, SCG signal and lung sound are easily detected using the ACM.

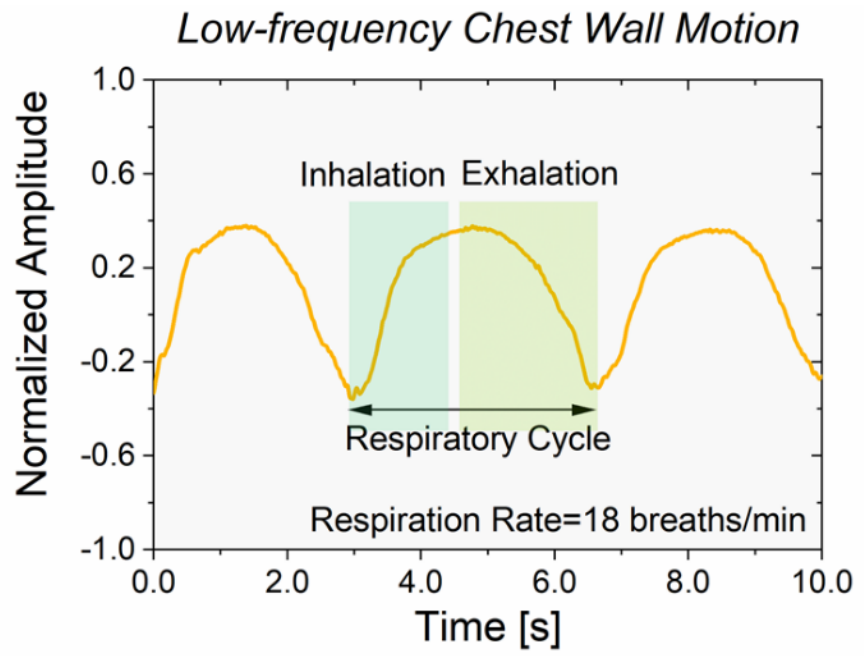


**Figure 25 – Low frequency chest wall motion showing the breathing pattern of an individual. Respiratory rate is calculated using this waveform.**

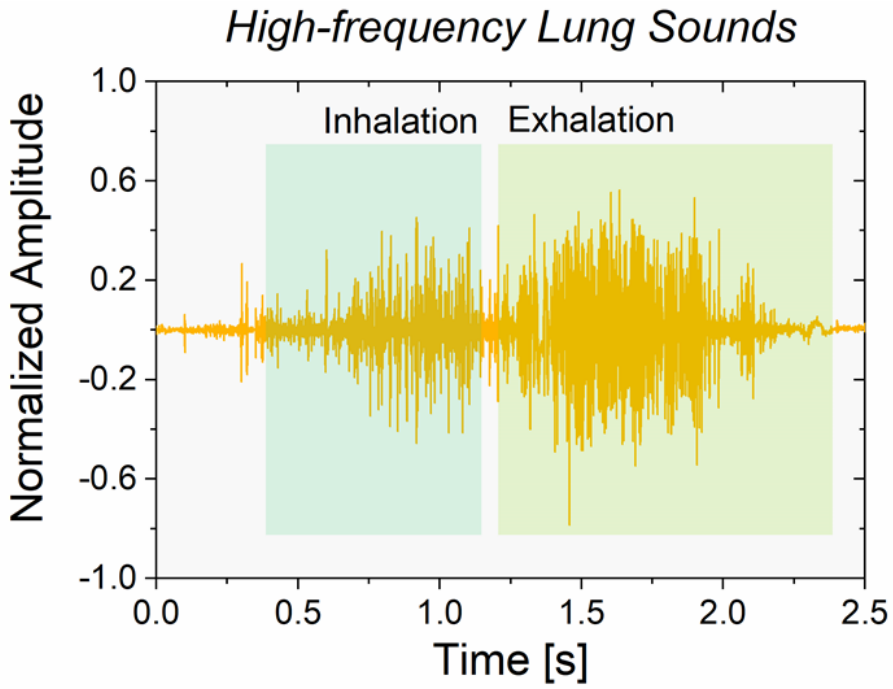


**Figure 26 – High frequency 'vesicular' lung sounds from a healthy subject. The sounds can be categorized based on their inhalation and exhalation phase within the respiratory cycle.**

### 4.3 Computed Health Parameters using the ACM

The sensor is applied to compute diagnostic parameters such as heart rate variability (HRV) and inter-beat intervals (IBIs) by extracting the time intervals based on the vibrational signatures of cardiac activities. Figure 27 displays the simultaneously recorded time domain signals of a medical-grade ECG alongside the ACM. Analogous to the R-peak of the ECG signal, the opening of the aortic valve is used as a reference peak to segment the recorded signal into individual beat components.

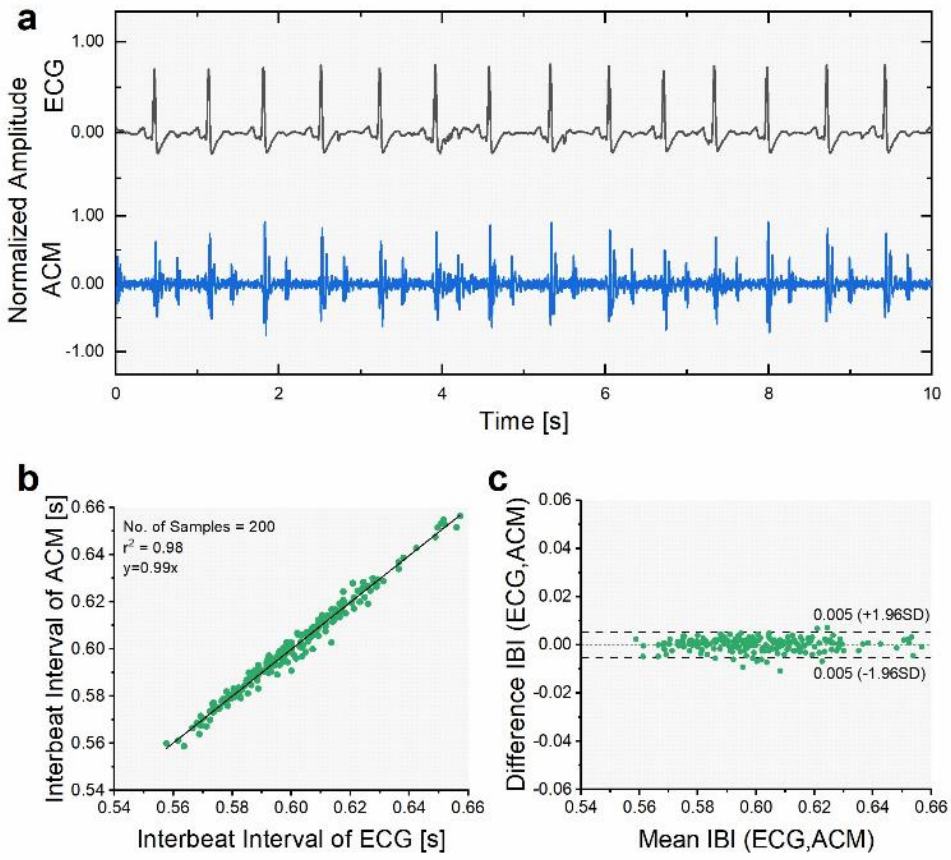


**Figure 27 – (a) Time domain plot of measured ECG signal alongside the ACM. (b) Correlation plot illustrating linear curve fit with $r^2 = 0.98$ confirming effective use of ACM for computation of diagnostic parameters (c) Bland-Altman plot comparing the technologies demonstrates 95% confidence interval having a range of 0.01s**

The IBIs calculated using the two methods demonstrates a high correlation, indicating a linear fit with $r^2$=0.98. A Bland-Altman plot quantifies this similarity showing the 95% confidence interval having a range of 0.01s. This signifies the use of the ACM for vital parameter monitoring in place of ECG electrodes without compromising on signal strength, quality, and accuracy, while providing additional benefits of auscultatory ability simultaneously.

# CHAPTER 5. CONCLUSION

The growing demand for remote health monitoring and wearable technologies will necessitate the integration of sensors into smaller form-factor with increased functionality and precision performance. The presented accelerometer contact microphone, whose functionality and feasibility are validated by an on-body auscultation test to capture heart and lung sounds, along with simultaneous recording of SCG signals and chest wall motions, represents as a major step towards this goal. The ability to compute vital health parameters such as the heart rate and heart rate variability within a high confidence interval as compared to medical-grade ECG further supports the use of the ACM in wearable auscultation devices. By integrating the functionality of a microphone and an accelerometer in a single MEMS device, the cost of manufacturing wearable devices can be reduced significantly.

The functionality of the ACM can be further improved by optimizing the device design to achieve a higher sensitivity, along with packaging the ACM under low vacuum conditions for an extended operational bandwidth exceeding 10kHz. Development of a noise matched ASIC will enable a lower noise performance of the sensor, allowing detection of weak pathological mechano-acoustic signatures from the body. Integrated packaging of the ACM sensor and ASIC will facilitate a miniaturized footprint and allow mechano-acoustic monitoring of several body parts, including knee joint sounds and abdominal bruits. Additional degrees of freedom of motion sensing can be added to the same die, e.g. a tri-axial wide-bandwidth micro-g accelerometer can be implemented using the same process platform technology, enabling motion capture along all orthogonal.

Implementation of classification and machine learning algorithms can simplify the data processing and provide objective quantification to cardiac health parameters which is currently unfeasible using conventional or electronic stethoscopes. Development of a wireless data acquisition system around the ACM will further increase the usability of the device during ambulatory conditions, such as during a stress test, allowing physicians to closely monitor the changes in the mechano-acoustic vibrations as the body undergoes physical activity. Using this device, a physician can observe cardiopulmonary health remotely with higher accuracy and precision.

# REFERENCES


[1] M. W. Bloom *et al.*, "Heart failure with reduced ejection fraction," *Nat. Rev. Dis. Prim.*, vol. 3, p. 17058, Aug. 2017.

[2] E. J. Benjamin *et al.*, "Heart Disease and Stroke Statistics-2019 Update: A Report From the American Heart Association," *Circulation*, 2019.

[3] J. A. Kirk *et al.*, "Pacemaker-induced transient asynchrony suppresses heart failure progression," *Sci. Transl. Med.*, vol. 7, no. 319, pp. 319ra207-319ra207, Dec. 2015.

[4] G. de Couto, M. Ouzounian, and P. P. Liu, "Early detection of myocardial dysfunction and heart failure," *Nat. Rev. Cardiol.*, vol. 7, p. 334, May 2010.

[5] S. Swarup and A. N. Makaryus, "Digital stethoscope: Technology update," *Medical Devices: Evidence and Research*. 2018.

[6] S. Leng, R. S. Tan, K. T. C. Chai, C. Wang, D. Ghista, and L. Zhong, "The electronic stethoscope," *BioMedical Engineering Online*. 2015.

[7] M. Sarkar, I. Madabhavi, N. Niranjan, and M. Dogra, "Auscultation of the respiratory system," *Ann. Thorac. Med.*, vol. 10, no. 3, pp. 158–168, 2015.

[8] Y. Seo, D. Corona, and N. A. Hall, "On the theoretical maximum achievable signal-to-noise ratio (SNR) of piezoelectric microphones," *Sensors Actuators, A Phys.*, 2017.

[9] S. Dornbush and A. E. Turnquest, *Physiology, Heart Sounds*. 2020.

[10] S. McGee, *Evidence-Based Physical Diagnosis*. 2012.

[11] K. N. Priftis, L. J. Hadjileontiadis, and M. L. Everard, *Breath sounds From basic science to clinical practice*. 2018.

[12] J. Kim, A. S. Campbell, B. E.-F. de Ávila, and J. Wang, "Wearable biosensors for healthcare monitoring," *Nat. Biotechnol.*, vol. 37, no. 4, pp. 389–406, 2019.

[13] J. M. Pevnick, K. Birkeland, R. Zimmer, Y. Elad, and I. Kedan, "Wearable technology for cardiology: An update and framework for the future," *Trends Cardiovasc. Med.*, vol. 28, no. 2, pp. 144–150, 2018.

[14] S. R. Steinhubl *et al.*, "Effect of a Home-Based Wearable Continuous ECG Monitoring Patch on Detection of Undiagnosed Atrial Fibrillation: The mSToPS Randomized Clinical TrialEffect of a Home-Based Wearable Electrocardiographic Patch on Detecting Atrial FibrillationEffect of a Hom," *JAMA*, vol. 320, no. 2, pp. 146–155, Jul. 2018.

[15] J. Dunn, R. Runge, and M. Snyder, "Wearables and the medical revolution," *Per. Med.*, vol. 15, no. 5, pp. 429–448, Sep. 2018.

[16] S. R. Steinhubl, E. D. Muse, and E. J. Topol, "The emerging field of mobile health," *Sci. Transl. Med.*, vol. 7, no. 283, pp. 283rv3-283rv3, Apr. 2015.

[17] O. T. Inan *et al.*, "Novel Wearable Seismocardiography and Machine Learning Algorithms Can Assess Clinical Status of Heart Failure Patients," *Circ. Heart Fail.*, 2018.

[18] Y. Liu *et al.*, “Epidermal mechano-acoustic sensing electronics for cardiovascular diagnostics and human-machine interfaces,” *Sci. Adv.*, vol. 2, no. 11, p. e1601185, Nov. 2016.

[19] A. Bohadana, G. Izbicki, and S. S. Kraman, “Fundamentals of Lung Auscultation,” *N. Engl. J. Med.*, vol. 370, no. 8, pp. 744–751, Feb. 2014.

[20] “Cardiac auscultation. A cost-effective diagnostic skill,” *Curr. Probl. Cardiol.*, 1995.

[21] H. B. SPRAGUE and P. A. ONGLEY, “The clinical value of phonocardiography.,” *Circulation*, 1954.

[22] R. Patel, D. L. Bushnell, and P. A. Sobotka, “Implications of an audible third heart sound in evaluating cardiac function,” *West. J. Med.*, vol. 158, no. 6, pp. 606–609, Jun. 1993.

[23] M. H. Drazner, J. E. Rame, L. W. Stevenson, and D. L. Dries, “Prognostic Importance of Elevated Jugular Venous Pressure and a Third Heart Sound in Patients with Heart Failure,” *N. Engl. J. Med.*, vol. 345, no. 8, pp. 574–581, Aug. 2001.

[24] A. Taebi, E. B. Solar, J. A. Bomar, H. R. Sandler, and A. H. Mansy, “Recent Advances in Seismocardiography,” *Vibration* , vol. 2, no. 1. 2019.

[25] C. A. Wick, J. H. McClellan, O. T. Inan, and S. Tridandapani, “Seismocardiography-based detection of cardiac quiescence for cardiac computed tomography

angiography," in *2014 36th Annual International Conference of the IEEE Engineering in Medicine and Biology Society, EMBC 2014*, 2014.

[26] J. Hansen-Honeycutt, E. B. Chapman, A. Nasypany, R. T. Baker, and J. May, "A Clinical Guide to the Assessment and Treatment of Breathing Pattern Disorders in the Physically Active: Part 2, a Case Series," *Int. J. Sports Phys. Ther.*, 2016.

[27] A. M. Brooks, J. T. McBride, K. M. McConnochie, M. Aviram, C. Long, and C. B. Hall, "Predicting deterioration in previously healthy infants hospitalized with respiratory syncytial virus infection," *Pediatrics*, 1999.

[28] J. J. Gilmartin and G. J. Gibson, "Abnormalities of chest wall motion in patients with chronic airflow obstruction," *Thorax*, 1984.

[29] J. P. McFadden, R. Price, H. D. Eastwood, and R. Briggs, "Raised respiratory rate in elderly patients: A valuable physical sign," *Br. Med. J. (Clin. Res. Ed).*, 1982.

[30] M. Chu *et al.*, "Respiration rate and volume measurements using wearable strain sensors," *npj Digit. Med.*, 2019.

[31] G. Z. Liu, Y. W. Guo, Q. S. Zhu, B. Y. Huang, and L. Wang, "Estimation of respiration rate from three-dimensional acceleration data based on body sensor network.," *Telemed. J. E. Health.*, 2011.

[32] K. Pandia, O. T. Inan, G. T. A. Kovacs, and L. Giovangrandi, "Extracting respiratory information from seismocardiogram signals acquired on the chest using a miniature accelerometer," *Physiol. Meas.*, 2012.

[33] K. Z. SIEJKO, P. H. THAKUR, K. MAILE, A. PATANGAY, and M.-T. OLIVARI, "Feasibility of Heart Sounds Measurements from an Accelerometer within an ICD Pulse Generator," *Pacing Clin. Electrophysiol.*, vol. 36, no. 3, pp. 334–346, Mar. 2013.

[34] H. Wen *et al.*, "Wafer-level-packaged HARPSS+ MEMS platform: Integration of robust timing and inertial measurement units (TIMU) on a single chip," in *2018 IEEE/ION Position, Location and Navigation Symposium (PLANS)*, 2018, pp. 261–266.

[35] H. Wen *et al.*, "A high-performance single-chip timing and inertial measurement unit with robust mode-matched gyroscopes," in *Proceedings of the IEEE International Conference on Micro Electro Mechanical Systems (MEMS)*, 2018.

[36] Y. Jeong, D. E. Serrano, and F. Ayazi, "Low-Pressure Wafer-Level-Packaged Capacitive Accelerometers With High Dynamic Range and Wide Bandwidth Using Nano-Gap Sloped Electrode Design," *J. Microelectromechanical Syst.*, vol. 26, no. 6, pp. 1335–1344, 2017.

[37] P. Gupta, Y. Jeong, J. Choi, M. Faingold, and F. Ayazi, "Precision High-Bandwidth Out-of-Plane Accelerometer As Contact Microphone for Body-Worn Auscultation Devices," 2018, pp. 30–33.

[38] Y. Jeong, A. Daruwalla, H. Wen, and F. Ayazi, "An out-of-plane 'hinge-shaped' nano-gap accelerometer with high sensitivity and wide bandwidth," in *TRANSDUCERS 2017 - 19th International Conference on Solid-State Sensors,*

*Actuators and Microsystems*, 2017.

[39] S. Reichert, R. Gass, C. Brandt, and E. Andrès, "Analysis of Respiratory Sounds: State of the Art," *Clin. Med. Circ. Respirat. Pulm. Med.*, 2008.

[40] S. R. Messer, J. Agzarian, and D. Abbott, "Optimal wavelet denoising for phonocardiograms," *Microelectronics J.*, 2001.

[41] Z. Syed, D. Leeds, D. Curtis, F. Nesta, R. A. Levine, and J. Guttag, "A framework for the analysis of acoustical cardiac signals," *IEEE Trans. Biomed. Eng.*, 2007.

[42] R. A. Wilson, V. S. Bamrah, J. Lindsay, M. Schwaiger, and J. Morganroth, "Diagnostic accuracy of seismocardiography compared with electrocardiography for the anatomic and physiologic diagnosis of coronary artery disease during exercise testing," *Am. J. Cardiol.*, 1993.